

ULTRA-FAINT DWARF GALAXIES: A CASE STUDY OF PEGASUS III AND PISCES II

Hannah Richstein¹ & Nitya Kallivayalil¹

¹*Department of Astronomy*

University of Virginia

Charlottesville, VA 22904, USA

April 8, 2022

ABSTRACT

Ultra-faint dwarf (UFD) galaxies are among the oldest, least chemically-enriched, most dark matter dominated stellar populations discovered to date. They also inhabit some of the least massive dark matter (DM) halos. While we cannot yet directly characterize these halos, we can use more easily measured properties such as half-light radius and luminosity to explore the UFD population as a whole, as well as to compare them to simulated analogs to see how well their DM prescriptions can reproduce observed characteristics. Here, we present deep *Hubble Space Telescope (HST)* photometry of the UFDs Pegasus III (Peg III) and Pisces II (Psc II), two of the most distant satellites in the halo of the Milky Way (MW). We measure the structure of both galaxies, derive mass-to-light ratios with newly determined absolute magnitudes, and compare our findings to expectations from UFD-mass simulations. We do not find any morphological features that indicate a significant interaction between the two has occurred, or that their morphologies are distinct from those of satellites closer to the Galactic Center. Future in-depth studies of UFDs will help characterize the population as a whole and give us insight into these darkest of galaxies and their fascinating histories.

1 Introduction

Ultra-faint dwarf (UFD) galaxies are the most dark-matter-dominated systems discovered, and thus a preferred laboratory for studying how well cosmological models predict behavior on small scales. The widely accepted Lambda Cold Dark Matter (Λ CDM) model uses the hierarchical accretion of low-mass systems to explain the growth of dark matter halos (e.g., Navarro et al., 1997). As UFDs occupy the least-massive dark matter halos discovered, they could be considered remnants of this hierarchical process while themselves having the simplest assembly histories.

The dark matter halos in which UFDs reside have extrapolated virial masses of approximately $10^9 M_{\odot}$ (e.g., Strigari et al., 2008), about two orders of magnitude smaller than where the Λ CDM theory predicts central dark matter densities in apparent contrast with observations. For example, in the mid-1990s, the cusp-core issue arose when observations of dwarf spiral galaxies showed cored mass distributions rather than the cusps predicted by dark-matter-only simulations (e.g., Flores & Primack, 1994; Moore, 1994).

It will take more information than we currently have, however, such as the shape of the velocity distribution or galactic internal proper motions (PMs), in addition

to radial velocities to be able to distinguish a dark matter central core or cusp (e.g., Strigari et al., 2007; Read et al., 2021; Guerra et al., 2021). Once we have full kinematic information, current virial mass estimators can be extended to further constrain UFD dark matter halo properties (Errani et al., 2018). In the meantime, we can use more UFD properties that are more readily determined, such as half-light radius and luminosity, to explore the population as a whole, as well as to compare them to simulations that resolve to their mass scale.

Defined by having M_V values fainter than -7.7 (e.g., Bullock & Boylan-Kolchin, 2017; Simon, 2019), UFDs went undetected until the advent of large-scale digital sky surveys, beginning with the Sloan Digital Sky Survey in 2005 (SDSS; York et al. 2000; Willman et al. 2005). Currently, over 21 UFDs have been spectroscopically verified, and more than 20 other candidates have been identified (e.g., Simon, 2019). These numbers are expected to increase further with the beginning of data collection at the Vera C. Rubin Observatory. While there is much to learn from studying any of these faint satellites, examining the relatively isolated UFDs at larger Galactocentric distances is particularly useful, as their current environments are more comparable to those produced in most simulations that resolve down to the UFD-mass level ($M_{\text{vir}} \simeq 10^9 M_{\odot}$ at $z=0$) (e.g., Jeon et al., 2017,

2021a,b; Wheeler et al., 2019). More recently, Applebaum et al. (2021) and Grand et al. (2021) were also able to resolve down to UFD-mass scale using cosmological MW zoom-in simulations. Comparing the properties of observed UFDs to both of these types of simulations could help us to disentangle the effects that host galaxies may have on their satellite UFDs.

Pegasus III (Peg III) is located at a heliocentric distance of approximately 215 kpc ($R_{GC} \sim 213$ kpc; Kim et al. 2016) and is thus one of the most distant MW UFDs known. Peg III was reported in Kim et al. (2015), having been discovered in Data Release 10 of SDSS (Ahn et al., 2014) and confirmed with the Dark Energy Camera (DECam). The discovery team noted the proximity (~ 30 kpc projected and ~ 32 kpc line-of-sight separation) of Peg III to Pisces II (Psc II; $R_{\odot} \sim 183$ kpc, $R_{GC} \sim 182$ kpc; Belokurov et al. 2010; Sand et al. 2012) at the time and suggested the possibility of an association (Kim et al., 2015). In a follow-up paper using Magellan/IMACS for photometry and Keck/DEIMOS for spectroscopy, Kim et al. (2016) derived a radial velocity for Peg III that, in the Galactic standard-of-rest (GSR), only differed from that of Psc II by ~ 10 km s $^{-1}$ (-67.6 ± 2.6 and -79.9 ± 2.7 km s $^{-1}$ (Kirby et al., 2015), respectively), and calculated a 3D-separation of ~ 43 kpc. Their team also found Peg III to have an irregular shape elongated in the direction of Psc II.

More recently, Garofalo et al. (2021) used the Large Binocular Telescope (LBT) to study variable stars in both UFDs. Using isodensity contour maps, they found no support for a physical connection between Peg III and Psc II, as neither UFD appeared to have an irregular shape. They suggested that the regular structures of both UFDs eliminate the notion of a stellar stream or another clear link between them.

Here, we present new, deep *Hubble Space Telescope* (*HST*) imaging of Peg III and Psc II, allowing further exploration of how these two UFDs may or may not be associated. We produce photometric catalogs and derive structural parameters, integrated *V*-band magnitudes, and mass-to-light ratios. In Section 2, we present our data and describe how they were processed. We measure the structural parameters and calculate mass-to-light ratios in Section 3. We discuss our results and conclude in Sections 4 and 5, respectively.

2 *Hubble Space Telescope* Data

2.1 Observations

The observations of Peg III and Psc II were performed using the F606W and F814W filters of the *HST* Advanced Camera for Surveys (ACS) Wide Field Channel (WFC) as part of Treasury program GO-14734 (PI: Kallivayalil). Parallel, off-target fields were simultane-

ously taken with the Wide Field Camera 3 (WFC3) using the same filters on the UV/visible (UVIS) channel. The Peg III observations were taken on 2017 April 26 and 2017 May 2 using two orbits for F606W and two orbits for F814W. Psc II was observed between 2017 June 19 and 2017 July 12 with two orbits dedicated to each filter. Each pair of ACS exposures totaled 4744 s, while each WFC3 pair totaled 5117 s.

2.2 Reduction and Photometry

The images were processed and corrected for charge-transfer inefficiency (CTI) using the current ACS and WFC3 pipelines. In each filter, the four dithered images were combined using the DRIZZLE package (Fruchter & Hook, 2002) to create `drc` fits files. Jackknife resampling was performed on the separate dither images to create four three-dither-combined images for deriving empirical errors. We used the `photutils` (Bradley et al., 2020) routines `DAOStarFinder` and `aperture_photometry` to detect sources and calculate the flux inside four-pixel circular apertures.

Sources in the three-dither combined images went through the same aperture photometry pipeline and were matched across the four combinations in each filter using a 6-parameter linear transformation. To derive empirical errors, we took the standard deviation of the magnitudes of the sources found across all of the combined images. The sources were matched in the F606W and F814W filters, then matched to the `drc` source list using the same 6-parameter transformation.

We then accounted for the encircled energy corrections, converted the flux to STMAG, and matched sources between the two filters. The observed magnitudes were corrected for dust extinction and reddening using the `dustmaps` module (Green, 2018) with the Schlegel et al. (1998) maps and Schlafly & Finkbeiner (2011) recalibration. Finally, we converted the ACS and WFC3 photometry from STMAG filters to VEGAMAG *V* and *I*. The resulting color-magnitude diagrams (CMDs) and typical errors are shown in Figure 1.

To present the data and to explore the existence of the elongation in Peg III measured by Kim et al. (2016), we created a contour map of stellar number density by performing a kernel density estimate on the data using $67.4.''5 \times 4.''5$ bins. The left panel of Figure 2 shows the 10 levels as filled contours for Peg III. The contour map for Psc II is illustrated in the right panel of Figure 2, created using the same process as for the Peg III map. This is consistent with past density contour maps (e.g., Belokurov et al., 2010; Sand et al., 2012) as both show Psc II with more regular levels. Comparing Psc II to Peg III, we see that Psc II is more compact and has a higher peak smoothed surface density.

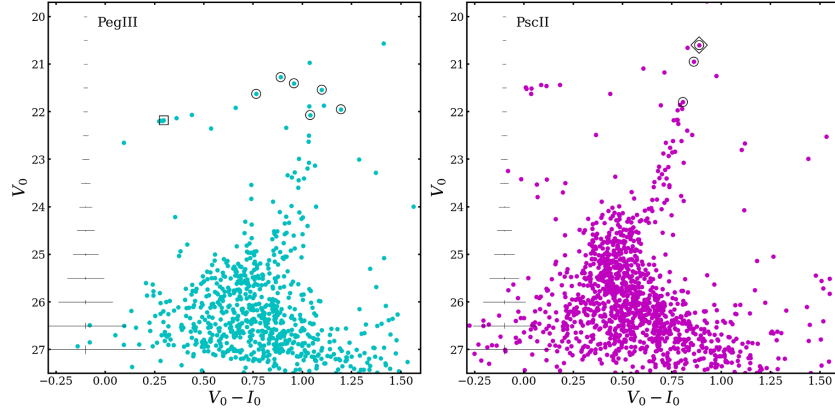


Figure 1: Color-magnitude diagrams of Pegasus III (left) and Pisces II (right) in VEGAMAG. The typical color and magnitude errors are shown to the left. Confirmed spectroscopic members in our catalog are shown in circles for Peg III, along with a star that has ambiguous membership in a square (Kim et al., 2016). There is one Peg III spectroscopic member that is not included in our catalog due to it falling within the ACS chip gap. The Psc II spectroscopic members with matches in our catalog are shown in circles (Kirby et al., 2015). Only 3 of the 7 member stars fall within the ACS field-of-view (FOV). The spectroscopic member with a *Gaia* proper motion (PM) is in the diamond. The other stars used in the Psc II PM measurement were either too bright or not in the ACS FOV.

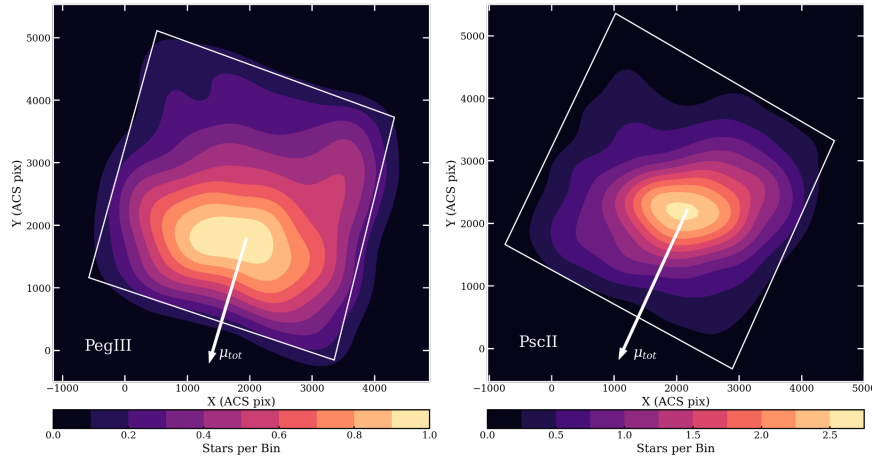


Figure 2: Density contour maps of Peg III (left) and Psc II (right). Each map shows 10 levels defined by the color bar and in units of stars per $4.''5 \times 4.''5$ bin. Note that the two color bars have different ranges and are not integer values as they are from kernel density estimates. The white lines show the borders of the ACS FOV, and the white arrows represent their total proper motions (μ_{tot}) over a timespan of 0.5 Myr from McConnell & Venn (2020). In this and all subsequent plots, the galaxies are oriented such that North is in the direction of the increasing y -axis and East is in the direction of the decreasing x -axis.

3 Structural Analysis

3.1 Fitting 2D-Profiles

To model the spatial structure of Peg III and Psc II, we followed the technique described in Drlica-Wagner et al. (2020) and Simon et al. (2021), largely based on the method shown in Martin et al. (2008). We modeled each UFD with exponential and Plummer (1911) profiles and performed binned Poisson maximum likelihood fits

to the probability density functions with the following free parameters: center position (x_0, y_0), richness (number of stars), 2D, projected semimajor axis of the ellipse that contains half of the total integrated surface density of the galaxy (elliptical half-light radius; a_h), ellipticity (ϵ), position angle of the semimajor axis measured East through North (θ), and background surface density (Σ_b). In past literature on these UFDs, the elliptical half-light radius a_h has often been referred to as r_h , but here we

have chosen to make the explicit distinction between a_h and the azimuthally-averaged half-light radius r_h (equal to $a_h\sqrt{1-\epsilon}$) for clarity and the purpose of our comparison to simulations.

The normalized functional forms of the exponential and Plummer profiles are as follows:

$$\Sigma_{\text{exp}}(r_i) = \frac{1}{2\pi r_e^2(1-\epsilon)} \exp\left(-\frac{r_i}{r_e}\right) \quad (1)$$

$$\Sigma_p(r_i) = \frac{r_p^2}{2\pi(1-\epsilon)} (r_i^2 + r_p^2)^{-2}. \quad (2)$$

Here, r_e and r_p are the scale lengths for each respective model, with $r_e=1.68a_h$ and $r_p=a_h$, and the first term in each equation is the normalization term, set to integrate to unity over all space. The r_i term is the elliptical radius of source i , defined as

$$r_i = \left\{ \left[\frac{1}{1-\epsilon} (X_i \cos\theta - Y_i \sin\theta) \right]^2 + (X_i \sin\theta + Y_i \cos\theta)^2 \right\}^{1/2} \quad (3)$$

X_i and Y_i are the spatial offsets from the centroid, where $X_i = x_i - x_0$ and $Y_i = y_i - y_0$.

To calculate the best-fitting parameters, we used the Markov chain Monte Carlo (MCMC) ensemble sampler `emcee` (Foreman-Mackey et al., 2013). We created $4.''5 \times 4.''5$ bins across the ACS field-of-view (FOV), masking the area of the chip gap and outside the FOV, and counted the number of stars in each bin. The values from this work and past works that measured structural parameters are shown in Tables 1 and 2 with the center position transformed from pixel space to coordinates in right ascension (RA) and declination (DEC). The spatially-binned, smoothed data, the smoothed best-fit exponential model, and the residuals are shown in Figures 3 and 4. After adding the background surface density term, we fit the following two functions:

$$\Sigma_{\text{exp,tot}}(r_i) = \Sigma_{\text{exp}}(r_i) + \Sigma_b \quad (4)$$

$$\Sigma_{p,\text{tot}}(r_i) = \Sigma_p(r_i) + \Sigma_b. \quad (5)$$

We show the best-fitting exponential and Plummer profiles for each galaxy (left: Peg III, right: Psc II) in Figure 5. Surface density measurements taken at 0.1 increments of the elliptical half-light radius are plotted against the elliptical radius R_e of each annular bin.

While the structural parameters we measured for Psc II are consistent with previous literature values, the a_h value of Peg III ($1.''88_{-0.33}^{+0.42}$) is much larger ($\sim 2.2\times$) than the most recent literature value from Kim et al. (2016) ($0.''85 \pm 0.22$, referred to as r_h in their paper). This can be seen in the leftmost panel of Figure 6. Here, we illustrate the best-fit 2D-exponential models

projected onto the sources in our FOV. The best-fit Plummer model from this work is shown as the dashed ellipse. The same comparisons are shown for Psc II, with the exponential fits shown in the middle panel and the Plummer fits in the right panel.

3.2 Magnitude Calculations

To derive the integrated magnitudes of each UFD, we opted for a probabilistic model approach as opposed to using discrete stars. To begin, we selected a box in color-magnitude space from $0 \leq (V-I) \leq 1.2$ and $20 \leq m_V \leq 29$. For both the on-field and off-field, we created a Gaussian kernel using `scikit-learn` (Pedregosa et al., 2011) `Kernel Density` and fit the kernel to the stars inside the color-magnitude box (CMD box). We gridded this space into 100 bins along each dimension, resulting in color bins ~ 0.01 dex and magnitude bins ~ 0.1 dex in width. We then generated random samples from the on- and off-field kernels and computed the log-likelihood of each sample under the model.

The off-field was used to create a probabilistic background model from which we estimated the excess flux. Integrating in both color and magnitude space, we calculated the stellar density in the CMD box by multiplying the log-likelihoods by the area of the CMD box and subtracting the off-field model from the on-field. The integral returned the flux of the stars inside the CMD box. We multiplied this flux by a correction factor derived from the exponential models to account for the flux outside the FOV. Converting this flux back to magnitude space yielded the integrated apparent magnitude.

This calculation was performed within a Monte Carlo simulation (MC) that included the individual source magnitude errors and FOV corrections calculated from different sets of model parameters. We report the median integrated m_V values of $17.50_{-0.21}^{+0.15}$ and 17.03 ± 0.04 for Peg III and Psc II, respectively, with the uncertainties representing the 16th and 84th percentiles. For the integrated M_V , we performed the same MC, this time also including errors on the distance modulus. We used the Kim et al. (2016) value of 21.66 ± 0.12 for Peg III and the Sand et al. (2012) 21.31 ± 0.17 value for Psc II, which gave the median values $M_V = -4.17_{-0.22}^{+0.19}$ for Peg III and $-4.28_{-0.16}^{+0.19}$ for Psc II, with the 16th and 84th percentiles quoted as the uncertainties.

3.3 Mass-to-Light Ratios

Using the newly derived elliptical half-light radii values, we calculate updated mass values using velocity dispersions from Kirby et al. (2015) and Kim et al. (2016). We use Equation 6 derived by Wolf et al. (2010), which was also employed by Kim et al. (2016) to estimate the mass within the elliptical half-light radius of Peg III. R_e is defined as the 2D-projected half-light radius from el-

Pegasus III			
Parameter	Kim et al. (2015)	Kim et al. (2016)	This Work
M_V	-4.1 ± 0.5	-3.4 ± 0.4	$-4.17^{+0.19}_{-0.22}$
<i>Exponential</i>			
RA (h:m:s)	$22:24:22.6 \pm 15''$	$22:24:24.48$	$22:24:25.82 \pm 5''$
DEC (d:m:s)	$+05:25:12 \pm 14''$	$+05:24:18.0$	$+05:24:54.01 \pm 3''$
θ_{exp} (deg)	133 ± 17	114^{+19}_{-17}	85 ± 8
ϵ_{exp}	$0.46^{+0.18}_{-0.27}$	$0.38^{+0.22}_{-0.38}$	$0.36^{+0.09}_{-0.10}$
$a_{h,\text{exp}}$ (arcmin)	$1.3^{+0.5}_{-0.4}$	0.85 ± 0.22	$1.88^{+0.42}_{-0.33}$
$a_{h,\text{exp}}$ (pc)	78^{+30}_{-24}	53 ± 14	118^{+31}_{-30}
<i>Plummer</i>			
RA (h:m:s)	-	-	$22:24:25.78 \pm 5''$
DEC (d:m:s)	-	-	$+05:24:54.17 \pm 3''$
θ_p (deg)	-	-	83^{+8}_{-7}
ϵ_p	-	-	$0.37^{+0.08}_{-0.09}$
$a_{h,p}$ (arcmin)	-	-	$1.67^{+0.26}_{-0.21}$
$a_{h,\text{exp}}$ (pc)	-	-	104^{+20}_{-23}

Table 1: Absolute magnitude and structural properties for Pegasus III, with the top six lines reporting the absolute V -band magnitude and best-fit exponential values and the bottom five listing the best-fit Plummer values. The uncertainties reported for RA, DEC, θ , ϵ , and a_h in arcminutes are the 16th and 84th percentiles from the MCMCs. The uncertainties on M_V and a_h in parsecs are the 16th and 84th percentiles from Monte Carlo simulations that took into account the errors on the distance modulus. Kim et al. (2015) and Kim et al. (2016) did not fit Plummer profiles to their data, and Kim et al. (2016) did not provide uncertainties on their central positions.

Pisces II				
Parameter	Belokurov et al. (2010)	Sand et al. (2012)	Muñoz et al. (2018)	This Work
M_V	-5.0 ± 0.5	-4.1 ± 0.4	-4.22 ± 0.38	$-4.28^{+0.19}_{-0.16}$
<i>Exponential</i>				
RA (h:m:s)	-	$22:58:32.33 \pm 5''$	$22:58:32.28 \pm 9''15$	$22:58:32.76 \pm 2''$
DEC (d:m:s)	-	$+05:57:17.7 \pm 4''$	$+05:57:09.36 \pm 5''7$	$+05:57:20.36 \pm 1''$
θ_{exp} (deg)	-	107	98 ± 13	97 ± 3
ϵ_{exp}	-	<0.28	0.39 ± 0.10	0.37 ± 0.04
$a_{h,\text{exp}}$ (arcmin)	-	1.09 ± 0.19	1.18 ± 0.20	$1.31^{+0.10}_{-0.09}$
$a_{h,\text{exp}}$ (pc)	-	58 ± 10	62.5 ± 10.6	69 ± 8
<i>Plummer</i>				
RA (h:m:s)	$22:58:31 \pm 6''$	$22:58:32.20 \pm 5''$	$22:58:32.28 \pm 9''15$	$22:58:32.75 \pm 2''$
DEC (d:m:s)	$+05:57:09 \pm 4''$	$+05:57:16.3 \pm 4''$	$+05:57:09.36 \pm 5''7$	$+05:57:19.96 \pm 1''$
θ_p (deg)	77 ± 12	110 ± 11	78 ± 20	98 ± 3
ϵ_p	0.4 ± 0.1	0.33 ± 0.13	0.34 ± 0.10	$0.37^{+0.03}_{-0.04}$
$a_{h,p}$ (arcmin)	1.1 ± 0.1	1.12 ± 0.18	1.12 ± 0.16	$1.34^{+0.08}_{-0.07}$
$a_{h,p}$ (pc)	$58 \pm 5^*$	60 ± 10	59.3 ± 8.5	71 ± 8

Table 2: Same as Table 1, for Pisces II. Belokurov et al. (2010) did not fit an exponential model to their data. Sand et al. (2012) had unconstrained uncertainties for the position angle in their exponential model and their reported ellipticity is the 68% upper confidence limit. *The uncertainty on the a_h in parsecs was derived for this work from a Monte Carlo simulation using the uncertainty on the a_h in arcminutes and the distance modulus of 21.3 reported in Belokurov et al. (2010).

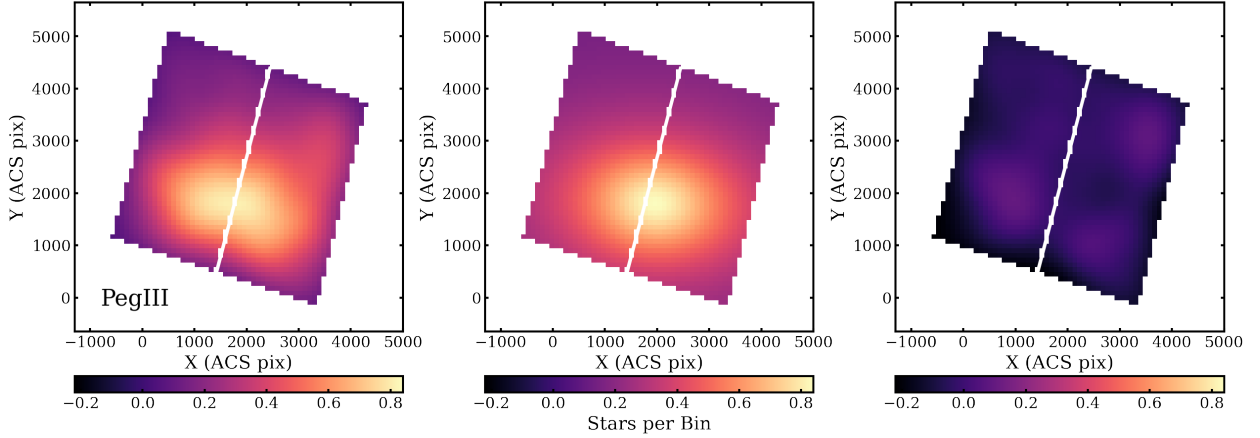


Figure 3: **Left:** Peg III data, smoothed using a Gaussian kernel with a FWHM of $0''.5$. **Middle:** Best-fitting exponential model, smoothed with a $0''.5$ FWHM Gaussian kernel. **Right:** The residuals between the smoothed data and the model.

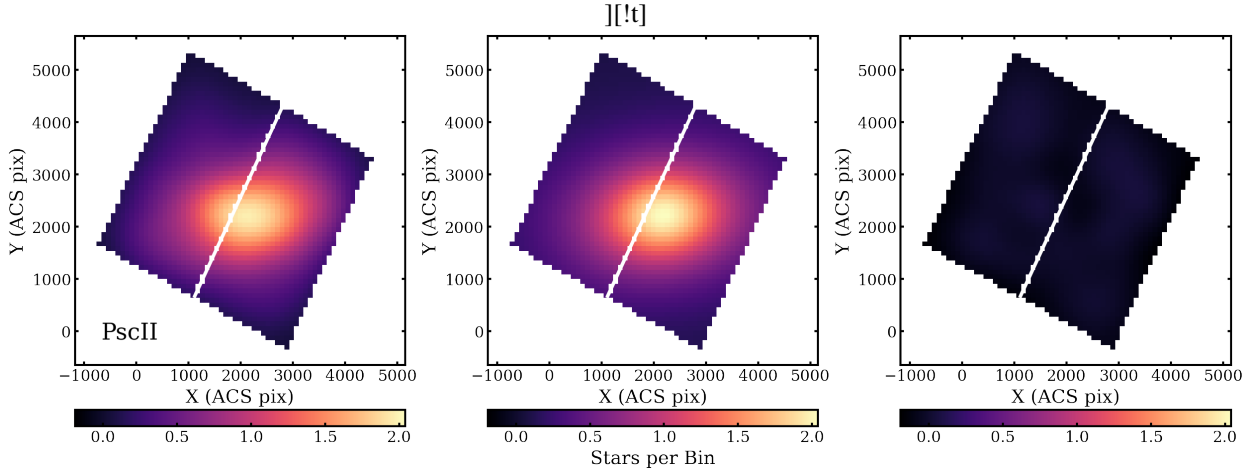


Figure 4: **Left:** Psc II data, smoothed using a Gaussian kernel with a FWHM of $0''.5$. **Middle:** Best-fitting exponential model, smoothed with a $0''.5$ FWHM Gaussian kernel. **Right:** The residuals between the smoothed data and the model.

lptical fits of surface brightness profiles and aligns with our a_h values.

$$M_{1/2} \simeq \frac{4}{G} \sigma_v^2 R_e \quad (6)$$

The Kim et al. (2016) $\sigma_v = 5.4_{-2.5}^{+3.0}$ km s $^{-1}$, determined using seven member stars, and our elliptical half-light radius measurement of 118 parsecs at 215 kpc gives a $M_{1/2} = 3.2_{-2.1}^{+4.3} \times 10^6 M_\odot$ for Peg III. Converting our M_V value to luminosity, we obtain the mass-to-light ratio within the elliptical half-light radius $(M/L_V)_{1/2} = 1600_{-580}^{+480} M_\odot/L_\odot$. This is within one sigma of the previously derived $1470_{-1240}^{+5660} M_\odot/L_\odot$ from Kim et al. (2016). Using the Kirby et al. (2015) $\sigma_v = 5.4_{-2.4}^{+3.6}$ km s $^{-1}$, which was also calculated using seven member stars, and our elliptical half-light radius of 69 parsecs at 183 kpc, we calculate a

$M_{1/2} = 1.9_{-1.3}^{+3.3} \times 10^6 M_\odot$ for Psc II. The $(M/L_V)_{1/2}$ is then $850_{-260}^{+570} M_\odot/L_\odot$. This agrees within two sigma with the value of $370_{-240}^{+310} M_\odot/L_\odot$ that Kirby et al. (2015) derived.

4 Discussion

Peg III and Psc II are among the few known UFDs in the outer halo of the MW, at Galactocentric distances of ~ 213 and ~ 182 kpc, respectively. To see how our measured Peg III and Psc II azimuthally-averaged half-light radius (r_h) and M_V values compare with those of other faint MW satellites, we place them in the size-luminosity plane (Figure 7). In addition to observed MW satellites (with a_h converted to r_h where necessary; McConnachie 2012; Muñoz et al. 2018), we have also included values from five sets of simulated UFDs: Jeon et al. (2017,

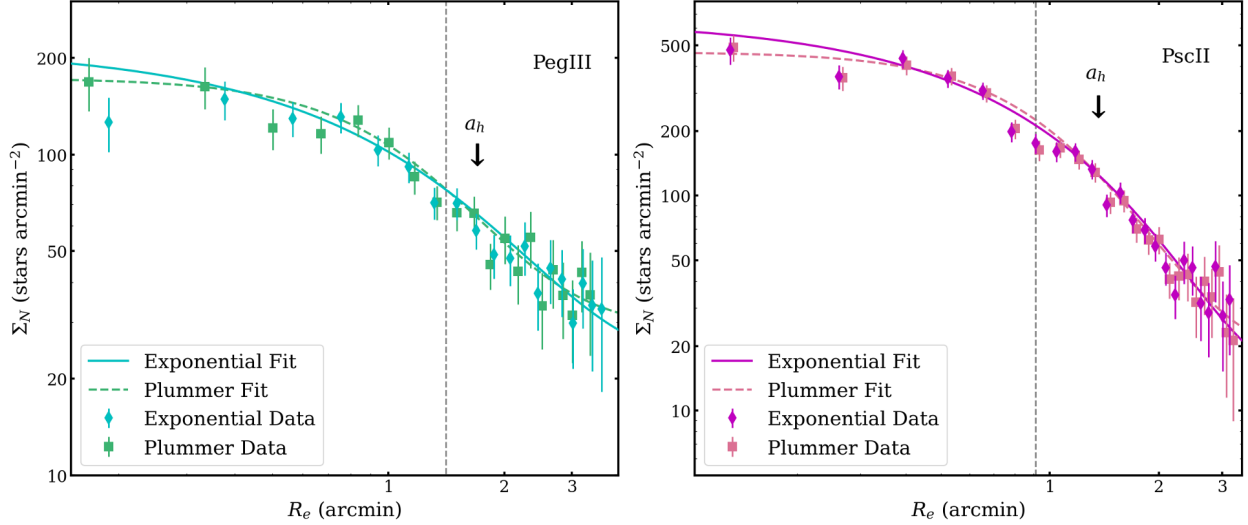


Figure 5: Best-fitting models for the surface density profiles of Pegasus III (left) and Pisces II (right) plotted against the elliptical radius. The curves show the best-fit one dimensional exponential (solid) and Plummer (dashed) profiles, which are fit to the full stellar distribution, not the annularly binned data shown here. The gray dashed line marks the approximate point where the elliptical annuli used for the surface density measurements begin to cover area outside the FOV in pixel space without source information in our catalogs. This was corrected for by dividing the number of stars in each elliptical annulus by only the area overlapping the FOV. The diamonds (squares) represent the surface density measurements in bins using the exponential (Plummer) model, with elliptical radii in increments of $0.1a_h$. The errors come from a Poisson distribution. The a_h marks the data points corresponding to the best-fit elliptical half-light radius.

2021a,b), Wheeler et al. (2019), and Applebaum et al. (2021). The observed satellites are split between two panels to explore the difference between those closer (left; <100 kpc) and farther (right; >100 kpc) from the Galactic Center. The simulated galaxies are shown in both panels, except for the Applebaum et al. (2021) values, which are split between the two according to their Galactocentric distances.

To derive M_V values for the Jeon et al. and Wheeler et al. (2019) simulations, we used Starburst99 (Leitherer et al., 1999) to convert from stellar mass and the given half-stellar-mass radii as (circular) half-light radii. The half-light radii that Applebaum et al. (2021) report are circular and derived from the summation of particle luminosities.

The Wheeler et al. (2019) simulations were unable to produce UFDs with half-light radii lower than 200 pc, which the authors suggested could be in tension with current observations because telescopes might only be sensitive to the “bright” cores of diffuse and relatively massive objects. Similarly, the Applebaum et al. (2021) simulations did not produce any galaxies in the UFD magnitude range with smaller r_h than ~ 300 pc, which may have been due to their force softening. Among the simulations included in our comparison, the Wheeler et al. (2019) and Jeon et al. (2021a,b) have the highest resolution,

with Wheeler et al. using $m_{\text{gas}}=30$ and $m_{\text{gas}}=250 M_\odot$ in their high- and median-resolution simulations, respectively, and Jeon et al. using $m_{\text{gas}}\sim 60 M_\odot$. As simulation techniques improve and are able to resolve a broader diversity of UFDs in a MW-environment, it will be interesting to see whether they more closely reproduce the scatter shown by McConnachie (2012) and Muñoz et al. (2018).

For Figure 7, we have imposed an upper magnitude limit of $M_V=-7.7$ to only include simulated galaxies in the UFD range, as Jeon et al. (2017), Wheeler et al. (2019), and Applebaum et al. (2021) produced galaxies in the dSph regime as well. As seen in Figure 7, Peg III and Psc II are well within the observed M_V and r_h ranges for other MW UFDs. They also fall in the range covered by the Jeon et al. (2021a,b) simulated field UFDs. Some closer MW UFDs and MW UFD candidates also fall within the simulated field UFD area, suggesting against this agreement being unique to outer-halo UFDs. Additionally, there is a higher number of observed satellites with smaller r_h and fainter M_v within 100 kpc, likely due to observational constraints.

As new observatories come online with deeper detection limits, smaller and fainter satellites beyond 100 kpc could be discovered that have no analogs in current simulations. One might expect outer-halo satellites that have

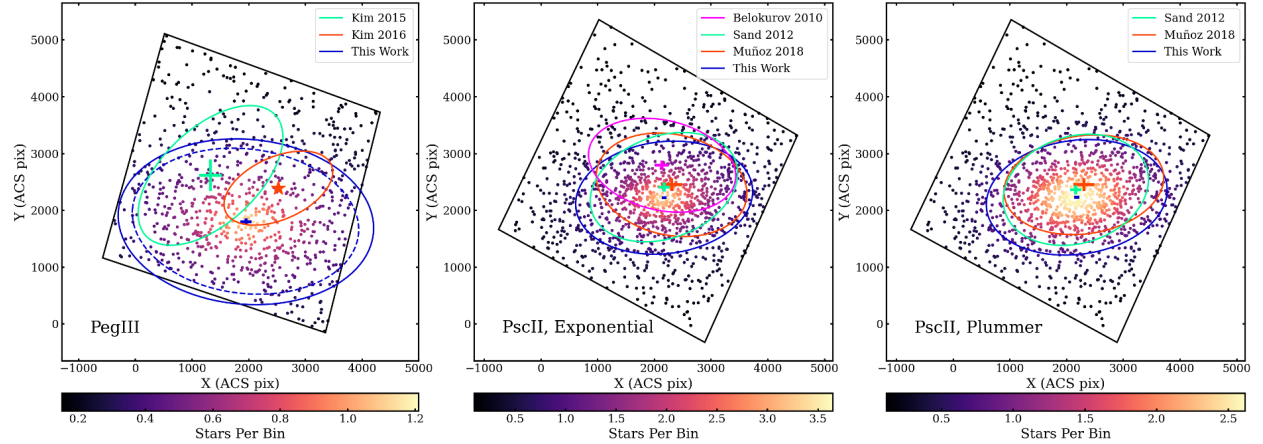


Figure 6: Comparison of past literature fits. Individual sources are colored based on the binned surface densities of the best-fitting exponential models in the left and center panels and the best-fitting Plummer model in the right panel. **Left:** Pegasus III. Exponential profile fits from Kim et al. (2015) and Kim et al. (2016) are shown in green and orange, respectively. The exponential profile fit from this work is shown in solid blue. The Plummer fit from this work is shown as the dashed blue ellipse. The central position is shown with error bars for Kim et al. (2015) in green and for this work’s exponential fit in blue. The central position from this work’s Plummer fit is not shown as it almost completely overlaps with the exponential value. The central position from Kim et al. (2016) is marked with an orange star, as no errors were reported. **Middle:** Exponential profile fits and central positions with error bars for Pisces II. Belokurov et al. (2010) is shown in fuchsia, Sand et al. (2012) in green, Muñoz et al. (2018) in orange, and this work in blue. **Right:** Plummer profile fits, with the same assigned colors as in the middle panel.

never been within 100 kpc of the MW to be more compact than UFDs with similar masses that have been closer and possibly subjected to strong tidal forces. If there are no or very few distant UFDs found in this smaller and fainter regime, the impact of the LMC and how it might have drawn UFDs closer (~ 50 kpc) at some point in their orbital history could be considered.

5 Conclusions

Based on deep *HST* imaging, we have measured the structural parameters for two distant MW UFD satellites, Peg III and Psc II. For this analysis, we used a 2D-maximum likelihood MCMC to fit exponential and Plummer profiles, finding central positions, elliptical half-light radii, ellipticities, position angles, number of stars, and surface background densities.

For Peg III, we measured an elliptical half-light radius of $1.88^{+0.42}_{-0.33}$ arcminutes, a position angle of 85 ± 8 degrees, and an ellipticity of $0.36^{+0.09}_{-0.10}$. The best-fit exponential model for Psc II gave an elliptical half-light radius of $1.31^{+0.10}_{-0.09}$ arcminutes, a position angle of 97 ± 3 degrees, and an ellipticity of 0.37 ± 0.04 . Our Psc II measurements are within 1σ agreement when compared to previous literature values, while we find a larger elliptical half-light radius value for Peg III. See Tables 1 and 2 for full comparisons. Future imaging of similar depth to ours paired with a larger FOV would help clarify the

true size of Peg III.

We compared the measured sizes and magnitudes of Peg III and Psc II to both those of other observed faint MW satellites and simulations of isolated field UFDs and satellite UFDs in a MW-like environment. While Peg III and Psc II are more distant MW UFDs with r_h and M_V values that correspond well to simulations of isolated field UFDs, they are not significantly distinct in structure from other observed UFDs in the inner MW halo. This could point to Peg III and Psc II (and other outer-halo UFDs) having been subject to tidal forces from the MW and/or the LMC throughout their lifetimes. Future morphological and kinematic analysis of more UFDs will help expand our understanding of the histories of these darkest of galaxies and how they came to be as we observe them today.

Acknowledgements

These data are associated with the *HST* Treasury Program 14734 (PI: Kallivayalil). Support for this program was provided by NASA through grants from the Space Telescope Science Institute. This material is based upon work supported by the National Science Foundation under grant No. AST-1847909. HR acknowledges support from the Virginia Space Grant Consortium Graduate Research STEM Fellowship. This research has made use of NASA’s Astrophysics Data System.

Parameter	Peg III	Psc II
$(m - M)_0$	21.66 ± 0.12	21.31 ± 0.17
v_{GSR} (km s ⁻¹)	-67.6 ± 2.6	-79.9 ± 2.7
σ_v (km s ⁻¹)	$5.4^{+3.0}_{-2.5}$	$5.4^{+3.6}_{-2.4}$
r_h (arcmin)	$1.51^{+0.35}_{-0.29}$	1.04 ± 0.08
r_h (pc)	94^{+25}_{-24}	55 ± 6
m_V	$17.50^{+0.15}_{-0.21}$	17.03 ± 0.04
$M_{1/2}$ (10 ⁶ M _⊙)	$3.2^{+4.3}_{-2.1}$	$1.9^{+3.3}_{-1.3}$
$(M/L_V)_{1/2}$ (M _⊙ /L _⊙)	1600^{+480}_{-580}	850^{+570}_{-260}

Table 3: Adopted and derived values for Peg III and Psc II. The Peg III distance modulus is from [Kim et al. \(2016\)](#), and the distance modulus for Psc II is from [Sand et al. \(2012\)](#). The σ_v values are from [Kim et al. \(2016\)](#) and [Kirby et al. \(2015\)](#) for Peg III and Psc II, respectively. The azimuthally-averaged half-light radius r_h is calculated using the relation $r_h = a_h \sqrt{1 - \epsilon}$. $(M/L_V)_{1/2}$ is the mass-to-light ratio within the elliptical half-light radius. The processes for the derivation of m_V , $M_{1/2}$, and $(M/L_V)_{1/2}$ are described in Sections 3.2 and 3.3. The uncertainties on all derived quantities are the 16th and 84th percentiles of Monte Carlo simulations including the full-error space of all the relevant terms.

Facility: HST (ACS,WFC3)

Software: Astrodizzle ([Fruchter & Hook, 2002](#)); Astropy ([Astropy Collaboration et al., 2013, 2018](#)); dustmaps ([Green, 2018](#)); emcee ([Foreman-Mackey et al., 2013](#)); Jupyter Notebook ([Kluyver et al., 2016](#)); Matplotlib ([Hunter, 2007](#)); Numpy ([Harris et al., 2020](#)); photutils ([Bradley et al., 2020](#)); scikit-learn ([Pedregosa et al., 2011](#)); Scipy ([Virtanen et al., 2020](#)); stsynphot ([STScI Development Team, 2020](#)); synphot ([STScI Development Team, 2018](#))

REFERENCES

- Ahn, C. P., Alexandroff, R., Allende Prieto, C., et al. 2014, *ApJS*, 211, 17
- Applebaum, E., Brooks, A. M., Christensen, C. R., et al. 2021, *ApJ*, 906, 96
- Astropy Collaboration, Robitaille, T. P., Tollerud, E. J., et al. 2013, *A&A*, 558, A33
- Astropy Collaboration, Price-Whelan, A. M., Sipőcz, B. M., et al. 2018, *AJ*, 156, 123
- Belokurov, V., Walker, M. G., Evans, N. W., et al. 2010, *ApJL*, 712, L103
- Bradley, L., Sipőcz, B., Robitaille, T., et al. 2020, *astropy/photutils: 1.0.0*, doi:10.5281/zenodo.4044744
- Bullock, J. S., & Boylan-Kolchin, M. 2017, *ARA&A*, 55, 343
- Drlica-Wagner, A., Bechtol, K., Mau, S., et al. 2020, *ApJ*, 893, 47
- Errani, R., Peñarrubia, J., & Walker, M. G. 2018, *MNRAS*, 481, 5073
- Flores, R. A., & Primack, J. R. 1994, *ApJL*, 427, L1
- Foreman-Mackey, D., Hogg, D. W., Lang, D., & Goodman, J. 2013, *PASP*, 125, 306
- Fruchter, A. S., & Hook, R. N. 2002, *PASP*, 114, 144
- Garofalo, A., Tantalò, M., Cusano, F., et al. 2021, arXiv e-prints, arXiv:2105.11488
- Grand, R. J. J., Marinacci, F., Pakmor, R., et al. 2021, *MNRAS*, 507, 4953
- Green, G. 2018, *The Journal of Open Source Software*, 3, 695
- Guerra, J., Geha, M., & Strigari, L. E. 2021, arXiv e-prints, arXiv:2112.05166
- Harris, C. R., Millman, K. J., van der Walt, S. J., et al. 2020, *Nature*, 585, 357
- Hunter, J. D. 2007, *Computing in Science & Engineering*, 9, 90
- Jeon, M., Besla, G., & Bromm, V. 2017, *ApJ*, 848, 85
- Jeon, M., Besla, G., & Bromm, V. 2021a, *MNRAS*, 506, 1850
- Jeon, M., Bromm, V., Besla, G., Yoon, J., & Choi, Y. 2021b, *MNRAS*, 502, 1
- Kim, D., Jerjen, H., Mackey, D., Da Costa, G. S., & Milone, A. P. 2015, *ApJL*, 804, L44
- Kim, D., Jerjen, H., Geha, M., et al. 2016, *ApJ*, 833, 16
- Kirby, E. N., Simon, J. D., & Cohen, J. G. 2015, *ApJ*, 810, 56
- Kluyver, T., Ragan-Kelley, B., Pérez, F., et al. 2016, in *Positioning and Power in Academic Publishing: Players, Agents and Agendas*, ed. F. Loizides & B. Schmidt (IOS Press), 87–90
- Leitherer, C., Schaerer, D., Goldader, J. D., et al. 1999, *ApJS*, 123, 3
- Martin, N. F., de Jong, J. T. A., & Rix, H.-W. 2008, *ApJ*, 684, 1075
- McConnachie, A. W. 2012, *AJ*, 144, 4
- McConnachie, A. W., & Venn, K. A. 2020, *Research Notes of the American Astronomical Society*, 4, 229
- Moore, B. 1994, *Nature*, 370, 629

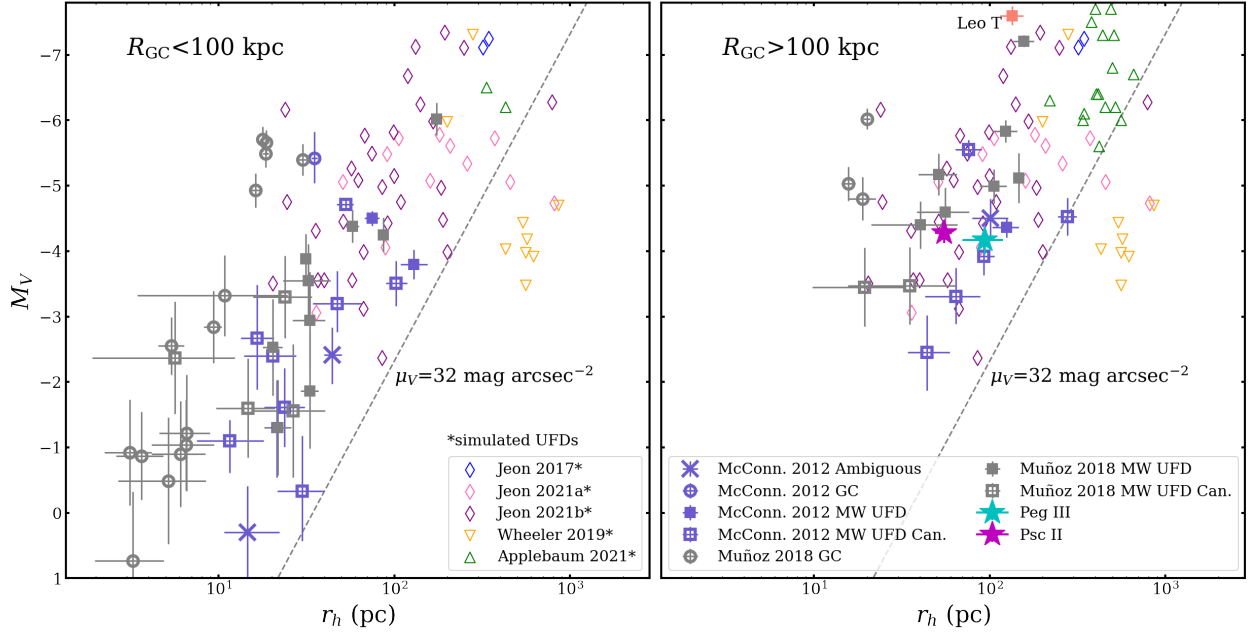


Figure 7: Comparison of simulated UFDs to observed MW satellites. The simulated UFDs (Jeon et al. 2017, blue diamonds; Jeon et al. 2021a, pink diamonds; Jeon et al. 2021b, purple diamonds; Wheeler et al. 2019, orange inverted triangles) are the same in both panels, except for the Applebaum et al. (2021) (green triangles), which are split between the two panels based on their simulated Galactocentric distances. Simulated UFDs can be distinguished from observed satellites as the latter all have error bars. The observed data are also split based on their Galactocentric distance, with satellites within 100 kpc shown in the left panel and satellites beyond 100 kpc in the right. Confirmed MW UFDs are shown as filled squares, candidate MW UFDs as open squares, MW globular clusters (GCs) as open circles, and ambiguous MW satellites as x's. The purple symbols use data from the updated McConnachie (2012) table, while the gray symbols (and Leo T, in orange) are from Muñoz et al. (2018). The dashed line represents a constant surface brightness of $32 \text{ mag arcsec}^{-2}$, approximately the current observational limit. Our measured Peg III (cyan star) and Psc II (magenta star) half-light radius and M_V values lie in the right panel, within the r_h and M_V range of other MW UFDs as well as the Jeon et al. (2021a,b) simulated field UFDs. Some inner-halo satellites from the left panel also fall within the Jeon et al. (2021a,b) range.

Muñoz, R. R., Côté, P., Santana, F. A., et al. 2018, *ApJ*, 860, 66
 Navarro, J. F., Frenk, C. S., & White, S. D. M. 1997, *ApJ*, 490, 493
 Pedregosa, F., Varoquaux, G., Gramfort, A., et al. 2011, *Journal of Machine Learning Research*, 12, 2825
 Plummer, H. C. 1911, *MNRAS*, 71, 460
 Read, J. I., Mamon, G. A., Vasiliev, E., et al. 2021, *MNRAS*, 501, 978
 Sand, D. J., Strader, J., Willman, B., et al. 2012, *ApJ*, 756, 79
 Schlafly, E. F., & Finkbeiner, D. P. 2011, *ApJ*, 737, 103
 Schlegel, D. J., Finkbeiner, D. P., & Davis, M. 1998, *ApJ*, 500, 525
 Simon, J. D. 2019, *ARA&A*, 57, 375
 Simon, J. D., Brown, T. M., Drlica-Wagner, A., et al. 2021, *ApJ*, 908, 18
 Strigari, L. E., Bullock, J. S., Kaplinghat, M., et al. 2007,

ApJ, 669, 676
 Strigari, L. E., Bullock, J. S., Kaplinghat, M., et al. 2008, *Nature*, 454, 1096
 STScI Development Team. 2018, synphot: Synthetic photometry using Astropy, ascl:1811.001
 STScI Development Team. 2020, stsynphot: synphot for HST and JWST, ascl:2010.003
 Virtanen, P., Gommers, R., Oliphant, T. E., et al. 2020, *Nature Methods*, 17, 261
 Wheeler, C., Hopkins, P. F., Pace, A. B., et al. 2019, *MNRAS*, 490, 4447
 Willman, B., Dalcanton, J. J., Martinez-Delgado, D., et al. 2005, *ApJL*, 626, L85
 Wolf, J., Martinez, G. D., Bullock, J. S., et al. 2010, *MNRAS*, 406, 1220
 York, D. G., Adelman, J., Anderson, John E., J., et al. 2000, *AJ*, 120, 1579